Lab Notes

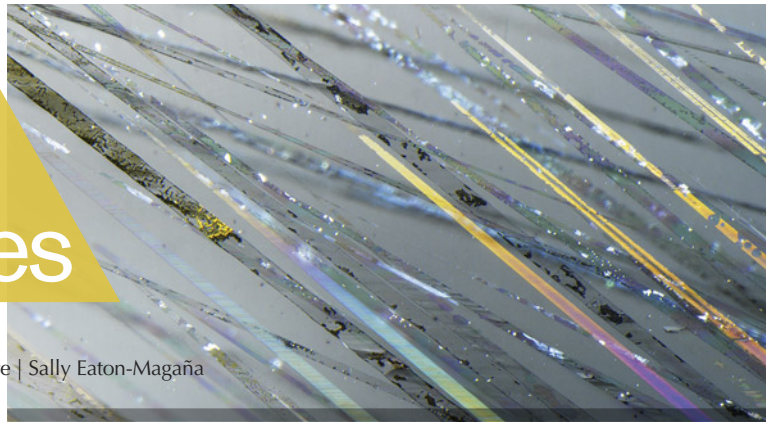

Editors
Thomas M. Moses | Shane F. McClure | Sally Eaton-Magaña

DIAMONDS

Cloud Inclusions Causing Fancy Light Blue Color in Diamond

The most common cause of blue color in diamond is the incorporation of boron into the diamond crystal lattice (type IIb), such as the recently auctioned Cullinan Blue (Summer 2022 Lab Notes, pp. 216–217). Other causes of blue color in diamond are hydrogen-related absorption (C.H. van der Bogert et al., "Gray-to-blue-to-violet hydrogen-rich diamonds from the Argyle mine, Australia," Spring 2009 *G&G*, pp. 20–37) and irradiation, either natural or artificial. Artificial irradiation using an electron beam is a common diamond treatment (Winter 2020 Lab Notes, pp. 517–518).

Recently submitted to the New York laboratory for colored diamond grading service was a 2.20 ct Fancy Light grayish blue diamond (figure 1). Compared to the Cullinan Blue, which was graded as Fancy Vivid blue on GIA's color grading scale, this diamond was type IIa (i.e., no boron) (figure 2). In addition to the absence of boron-related impurities, this diamond lacked any hydrogen-related impurities (observed in the ultraviolet/visible/near-infrared spectrum in figure 3) (van der Bogert et al., 2009) or any GR1-related color centers, thus ruling out these major causes of blue color in diamond. Instead, the UV absorption for the 2.20 ct diamond was similar to what would be expected for a yellow type Ib (isolated nitrogen) diamond (figure 3).

Figure 1. The 2.20 ct Fancy Light grayish blue diamond.

The diamond was heavily included with fine cloud-like inclusions, giving it a milky appearance (figure 4). Clouds, sometimes hydrogen-related, often cause gray, brown, black, or even white color in natural diamonds (S. Eaton-Magaña et al., "Natural-color fancy white and fancy black diamonds: Where color and clarity converge," Fall 2019 *G&G*, pp. 320–337). In this case, the cloud micro-inclusions caused Rayleigh light scattering, creating a desirable blue color and not the expected yellow color resulting from a slight rise in absorption from lower to higher energy.

Based on these cloud inclusions, the diamond was given a final color

Figure 2. The mid-infrared spectrum of type IIb diamond compared to the 2.20 ct grayish blue diamond, which was type IIa with no boron or hydrogen-related features. Spectra are offset vertically for clarity.

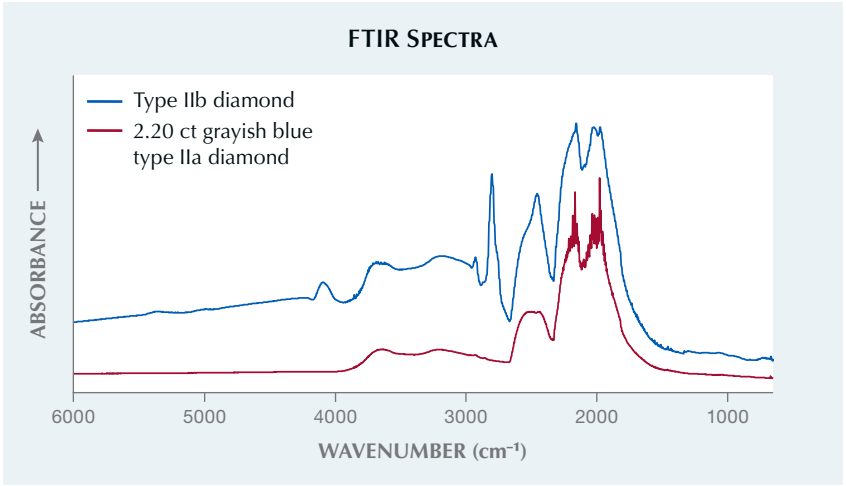

Editors' note: All items were written by staff members of GIA laboratories.

Gems & Gemology, Vol. 60, No. 1, pp. 58–72.

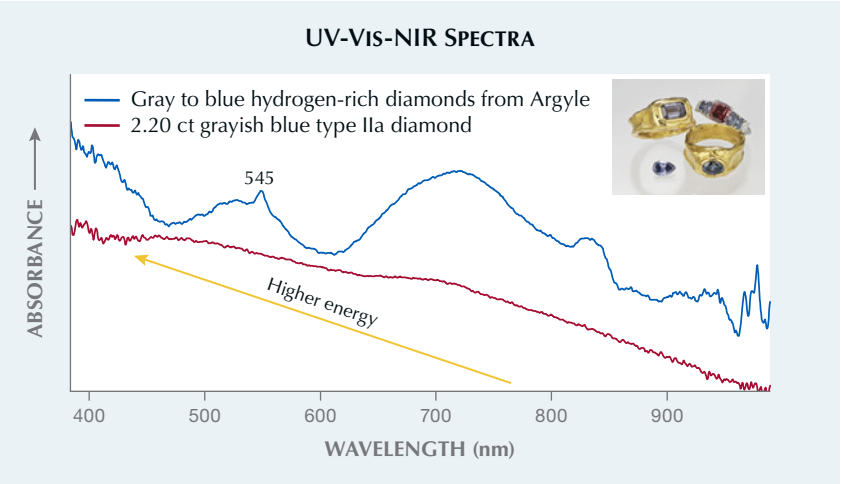

Figure 3. The UV-Vis-NIR spectrum of the 2.20 ct grayish blue diamond compared to a UV-Vis-NIR spectrum with typical hydrogen absorbance (notably at ~545 nm) and broad bands at ~700–800 nm, causing the desirable violet to blue colors. The inset shows typical colors associated with this absorbance spectrum. The red trace is also inconsistent with type IIb absorption. With a slight rise to higher energy, a yellow color is expected. Spectra are offset vertically for clarity.

grade of Fancy Light grayish blue, a natural origin of color, and an I_3 clarity grade.

Paul Johnson

Natural Orange Diamond with Unusual Absorption Features

Orange is a very desirable color for diamond in the gem trade. GIA's New York laboratory received two type Ia (nitrogen-bearing) orange diamonds for colored diamond grading service, one 0.16 ct Fancy Vivid orange and the other 0.23 ct Fancy Intense orange (figure 5). Both diamonds showed orange fluorescence to long-wave and short-wave UV, along with few inclusions (clarity grades of VS_2 and VVS_1, respectively) and strong color zoning related to crystal growth (figure 6).

This diamond hue is often caused by a broad-band absorption at 480 nm. While the 480 nm band was observed in both diamonds, it was supplemented by the presence of a 525 nm

Figure 5. A 0.16 ct Fancy Vivid orange pear (left) and 0.23 ct Fancy Intense orange pear (right).

Figure 4. Fine milky cloud inclusions are responsible for the natural blue color of the type IIa diamond, shown in dark-field illumination.

peak and the 550 nm band along with a series of absorption features from ~700 to 780 nm with pronounced peaks at 735, 753, and 769 nm (figure 7). The 830 nm photoluminescence (PL) spectra showed very strong nickel peaks at 883/884 nm, in addition to numerous other PL features (A.M. Zaitsev, *Optical Properties of Diamond: A Data Handbook*, Springer-Verlag, Berlin, 2001). Thus, the 480 nm band was not the exclusive cause of color. The 550 nm band is the most common cause of color in natural pink diamond but, when present with other color centers, can contribute to many different bodycolors.

The optical defects in these orange diamonds differed from those in diamonds exclusively colored by the 480 nm band (M.Y. Lai et al., "Spectroscopic characterization of diamonds colored by the 480 nm absorption band," *Diamond and Related Materials*, Vol.

Figure 6. Fancy Vivid orange color distribution with strong zoning related to crystal growth.

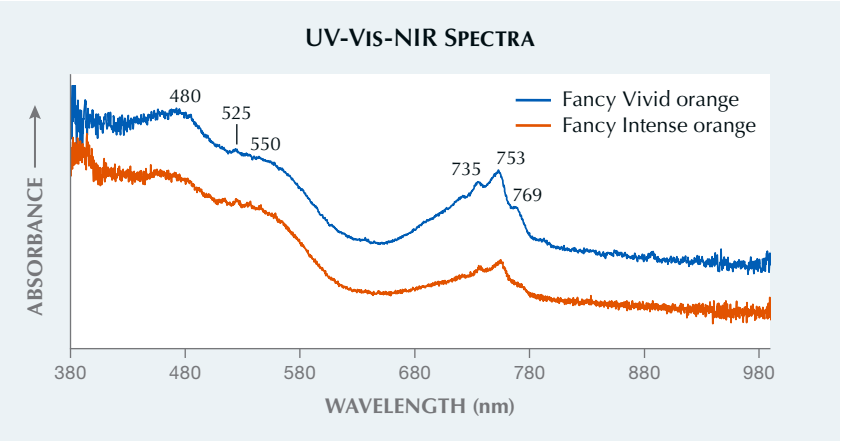

Figure 7. Ultraviolet/visible/near-infrared spectra of the Fancy Vivid orange and Fancy Intense orange diamonds are shown with several peaks and bands that combine to create these very rare colors. Spectra are offset vertically for clarity.

142, 2024, p. 110825). The combination of an unusual absorption band in the near infrared with the 480 and 550 nm absorption bands creates a transmission window that produces the rich, warm orange hue, devoid of any secondary modifying color. This appears to be a newly identified cause of orange color in diamonds.

A'Dhi Lall, Sally Ruan, and Paul Johnson

Dual-Color Double Chatoyancy in EMERALD

GIA's Tokyo laboratory recently received for origin service a ring with an emerald displaying dual-color double chatoyancy (figure 8). One band showed white chatoyancy, while the other exhibited greenish chatoyancy similar to the bodycolor. The emerald had an oval double-cabochon shape with a polished crown and pavilion and contained parallel tubes slightly oblique to the polished pavilion, resulting in semitransparency. The dual-color double chatoyancy was caused by the same mechanism identified in dual-color star corundum and quartz by Schmetzer et al. ("Dual-color double stars in ruby, sapphire, and quartz: Cause and historical account," Summer 2015 *G&G*, pp. 112–143). The white chatoyancy was caused by the linear reflection of the parallel tube inclusions from the upper cabochon surface. The greenish chatoyancy was caused by the linear reflection of the polished curved base through the interior of the stone to the surface (figure 9). Double chatoyancy is occasionally observed, but it is rare to find a very clear example of dual-color double chatoyancy.

Kazuko Saruwatari

Figure 8. The emerald in this ring displays dual-color light green and white double chatoyancy. The stone measures 8.39 × 5.71 × 4.22 mm.

Electroformed GOLD Bracelet

GIA has provided a service for validating mounted gemstones in jewelry for decades. Recently, these services have been expanded to include precious metal items (rings, necklaces, and bracelets) to ensure their authenticity and ensure the metal is as stated. The service is intended to protect both buyer and seller.

As part of this service, a gold bracelet measuring 8 inches in circumference and 1.25 inches wide and weighing 41 g was recently examined in the Carlsbad laboratory (figure 10). It was submitted as 14K solid gold, but initial observations raised suspicion. The bracelet felt too light and almost hollow, and there was a significant contrast in textures: a matte finish on the inside surface of the bracelet compared with the wavy, shiny exterior

Figure 9. Side view of the emerald ring. Parallel tube inclusions are oblique to the pavilion. The white reflection on the right is caused by the inclusions near the surface of the curved cabochon, while the greenish reflection on the left is caused by the reflection off of the bottom face of the cabochon.

Figure 10. The electroformed gold bracelet submitted as 14K solid gold.

Figure 11. The hallmark is not actually stamped onto the metal but is on a separate disk adhered to the inside of the bracelet.

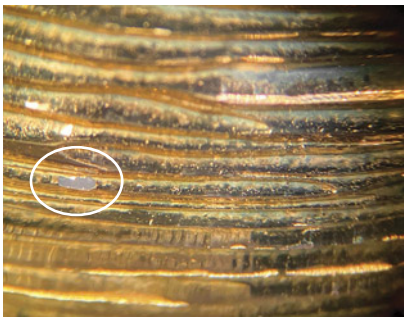

Figure 12. An area where the gold plating has flaked off from the bracelet is shown in the circled region.

surface. The bracelet had a 14K hallmark, which appeared to be stamped or engraved onto a different metal piece that was glued or otherwise adhered to the bracelet (figure 11).

X-ray fluorescence (XRF) analysis of the shiny exterior surface gave a result of 17.99K gold, and no subsurface material was detected that would indicate plating. Additional testing of another smooth surface yielded a result of 22.47K. Further analysis under brighter lighting conditions revealed areas where gold plating had flaked off from the piece (figure 12). We believe this wavy texture of the gold was used intentionally to hide the poor quality of the finish and the flaking gold plating, as shadows can often mask imperfections on initial sight.

A wax or resin material was observed under the plating, and we concluded that the bracelet had been created using electrodeposition to electroform the piece. Electroforming is a method of adding a thick gold plating, sometimes as thick as 200 microns, to a wax, resin, ceramic, or organic material base. Thick plating and electroforming may not be detected by XRF methods alone, and additional testing may be necessary to detect the application of these processes. We believe this wax- or resin-filled electroformed bracelet was being sold as solid 14K gold with the intention to deceive the buyer. This example demonstrates the importance of testing and verification services such as GIA's jewelry verification service.

Carlos Bautista and Paul Johnson

LABORATORY-GROWN DIAMONDS

CVD with "Ancient Text" Clouds

The Surat lab received a 1.67 ct D-color pear shape submitted for laboratory-grown diamond service. Spectroscopy and fluorescence imaging confirmed this was a diamond grown by chemical vapor deposition (CVD) that had undergone post-growth high-pressure, high-temperature (HPHT) annealing. This CVD diamond with SI_1 clarity displayed an interesting cloud feature that resembled lines of text in an ancient manuscript (figure 13).

The "lines" of clouds—a feature never before seen by the authors—were oriented approximately 45° to the growth interface seen with DiamondView imaging (figure 14). Examination of the fluorescence images (including those collected with selective-wavelength filters) revealed that the cloud features did not coincide with dislocation bundles, and striations were not observed. Photoluminescence mapping with 532 nm excitation showed high concentrations of the silicon vacancy (SiV^-) defect at 737 nm but did not indicate any spatial features corresponding to the clouds. Infrared absorption spectroscopy indicated a type IIb diamond with very low concentrations of uncompensated boron.

This diamond was noteworthy for its unusual and visually appealing clarity characteristic. Additionally, the dichotomy of a thoroughly modern diamond with a cloud feature that evoked an ancient text provided an interesting submission.

Sally Eaton-Magaña, Manisha Bhoir, and Girish Dodiya

Figure 13. The pavilion of this 1.67 ct pear-shaped CVD-grown diamond displayed an interesting feature with numerous cloud features resembling lines of text. Field of view ~2 mm.

Figure 14. A DiamondView image of the pavilion shows the region containing the cloud characteristic. While this image reveals the growth interfaces and the coloration confirms HPHT annealing, it does not show features corresponding to the cloud.

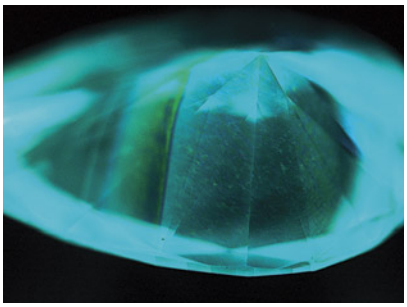

Figure 15. This 15.73 ct G-color CVD-grown diamond showed indications of HPHT treatment.

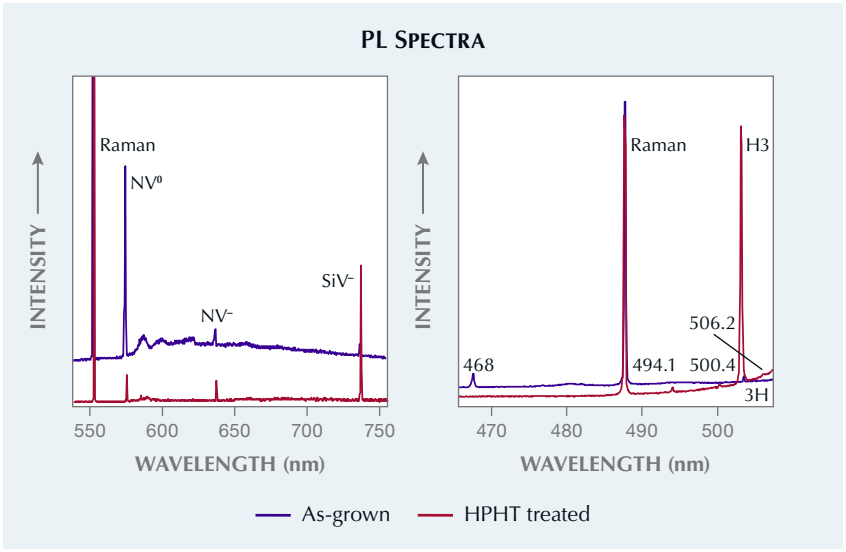

Figure 17. PL spectra collected on the CVD-grown diamond in January 2022 and recently with 514 nm (left) and 457 nm (right) excitation. Diamond Raman lines are scaled as equal, and spectra are offset vertically for clarity.

Large CVD-Grown Diamond Resubmitted after HPHT Treatment

In January 2022, the record holder for largest diamond grown by chemical vapor deposition (CVD) was a 16.41 ct square modified brilliant with G color and VVS_2 clarity that showed no indications of post-growth treatment (Spring 2022 Lab Notes, pp. 54–56). Recently, this diamond was resubmitted to the Carlsbad laboratory with a weight of 15.73 ct (figure 15). Standard data collection indicated that since the original submission, the stone had undergone high-pressure, high-temperature (HPHT) treatment. Consequently, this provided a case study showing the spectral and fluorescence differences between the as-grown and HPHT-treated versions. The color and clarity grades remained unchanged.

Although HPHT processing of CVD-grown diamonds is often performed to improve the color grade by reducing brown coloration (S. Eaton-Magaña and J.E. Shigley, "Observations on CVD-grown synthetic diamonds: A review," Fall 2016 *G&G*, pp. 222–245), the diamond displayed no observable color improvement. It is also likely that the HPHT treatment created frosting of the facets that required repolishing, which could partially account for the 0.68 ct weight loss.

Figure 16. DiamondView fluorescence images collected on the originally submitted CVD-grown diamond (left, from Spring 2022 Lab Notes) exhibited no evidence of post-growth treatment, while the recent submission (right) showed signs of HPHT treatment.

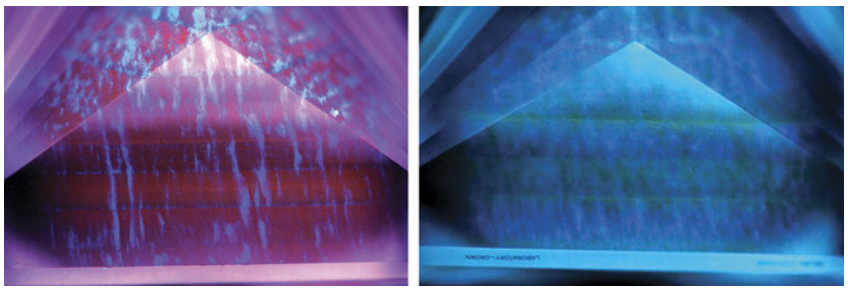

DiamondView fluorescence imaging showed pronounced differences between the as-grown and treated stages (figure 16). This color change in fluorescence imaging is often seen in HPHT-treated CVD-grown diamonds due to the reduction of nitrogen vacancy (NV) centers (NV^0 with zero-phonon line [ZPL] at 575 nm and NV^- at 637 nm) and an increase in H3 (NVN^0; ZPL at 503.2 nm). The changes in the defect concentrations leading to the differences in the fluorescence colors were also evident in photoluminescence (PL) spectroscopy collected at liquid nitrogen temperature. Figure 17 shows the PL results with 514 and 457 nm excitation for the 16.41 and 15.73 ct stages of the diamond.

With HPHT treatment, there was a decrease in the NV centers and an increase in the silicon vacancy (SiV^-) center at 737 nm in the 514 nm PL spectrum. In the 457 nm PL spectrum, the 468 nm peak and 3H peak (ZPL at 503.5 nm) were no longer detected, while features developed at 494.1, 500.4, and 506.2 nm along with the H3 peak at 503.2 nm.

As expected with a treated CVD-grown diamond, there were no major changes in many of the growth features. The cathodoluminescence images in figure 18 show no observable

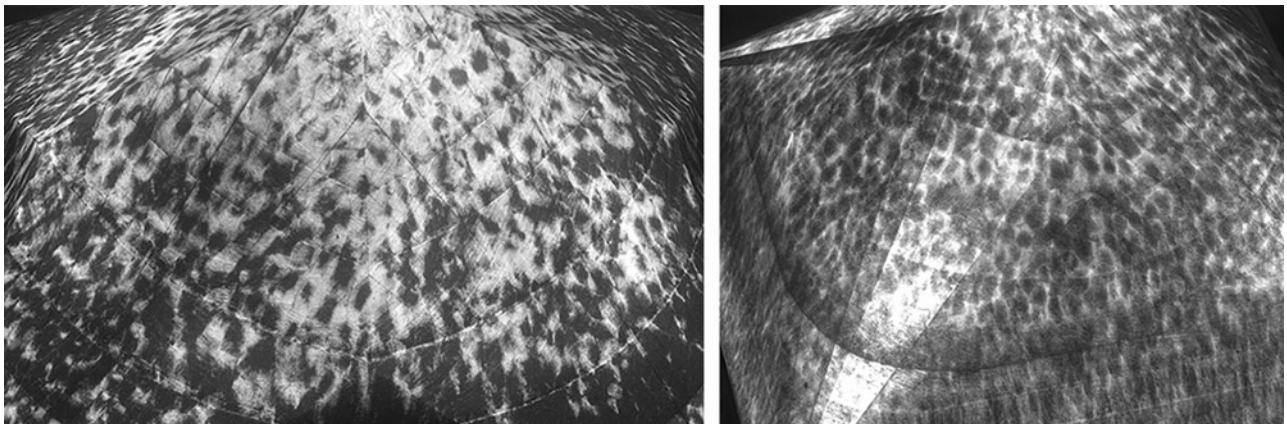

Figure 18. Comparison of the cathodoluminescence images from before HPHT treatment (left, from Spring 2022 Lab Notes) and afterward (right) showed no observable differences.

differences; the black dots are associated with lattice dislocations. The seven growth interfaces seen in figures 16 and 18 appear unmodified.

This stone allowed for an interesting comparison of a CVD-grown diamond before and after commercial HPHT treatment.

Sally Eaton-Magaña and Elina Myagkaya

PEARLS

Large Freshwater Cultured Pearls with Atypical Bead Nuclei

Freshwater cultured pearls are known for their wide range of attractive colors, including different combinations of white, orange, pink, and purple hues. In the past decade, round or near-round freshwater bead cultured pearls of large size, commonly called "Edison" pearls in the trade, have gained popularity (Summer 2015 Lab Notes, pp. 179–181; C. Zhou et al., "Detection of color treatment and optical brightening in Chinese freshwater 'Edison' pearls," Summer 2021 *G&G*, pp. 124–134). Recently, two necklaces consisting of large pearls of mostly orangy pink to purplish pink colors (figure 19), ranging in size from 15.40 to 17.42 × 16.70 mm and from 18.00 to 19.96 × 19.06 mm, were submitted to GIA's New York laboratory. The strands caught our attention for their size and intense colors, as well as the growth features found inside these pearls.

Real-time X-ray microradiography (RTX) revealed that all the pearls were bead cultured—but not with the shell bead nuclei typically used for cultured pearls. Instead, a more X-ray transparent material with a distinct outline and near-round shape was found inside them (figure 20). The material appeared porous and nonuniform and did not resemble the "mud-like" material found in "soufflé" freshwater cultured pearls previously studied (Spring 2010 Gem News International, pp. 61–63). However, the exact nature of this material could not be determined.

Figure 19. These two necklaces consisting of large freshwater cultured pearls displayed strong hues with orient. Courtesy of Yvel.

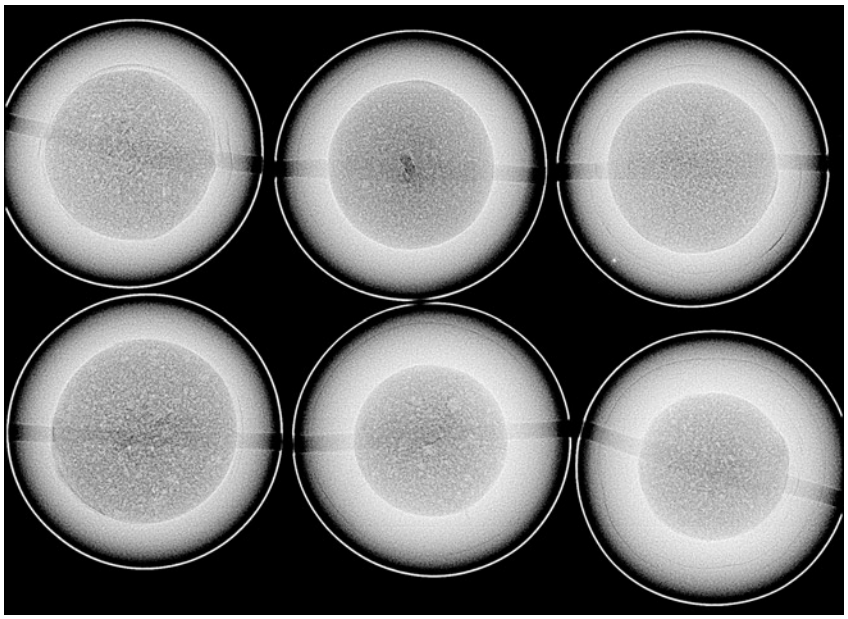

Figure 20. RTX analysis revealed the near-round atypical bead nucleus used to culture each of the pearls.

Energy-dispersive X-ray fluorescence analysis of their trace elemental concentrations (such as manganese and strontium) confirmed that the pearls were grown in a freshwater environment. Furthermore, Raman spectroscopy using 514 nm laser excitation indicated that their colors were natural, with two strong peaks around 1125 and 1510 cm^{-1} associated with natural polyenic pigment.

Cultured freshwater pearls with large size, near-round shape, and intense coloration are highly sought after and more valuable than traditional freshwater cultured pearls. These large freshwater cultured pearls are especially noteworthy because of the unique bead nuclei used during the culturing process, which suggests that culturing techniques are continuously evolving, resulting in higher-quality products.

Chunhui Zhou, Emiko Yazawa, and Madelyn Dragone

Figure 21. This 8.03 ct brown oval imitation pearl resembled a pen pearl at first glance.

Iridescent Imitation Pearl

An unusual brown oval specimen weighing 8.03 ct was recently submitted to GIA's Bangkok laboratory for pearl identification. At first sight, the material resembled a pen pearl due to its dark color and non-nacreous appearance (figure 21). Upon closer inspection, however, it lacked the cellular structure characteristic of such pearls (N. Sturman et al., "Observations on pearls reportedly from the Pinnidae family (pen pearls)," Fall 2014 *G&G*, pp. 202–215). It instead displayed a wispy, fibrous-like pattern and mosaic patches of iridescence, resembling a lava cave sheathed in spiderwebs (figure 22, left). Under fiber-optic illumination, the iridescence phenomenon was visible within the body and varied

Figure 22. Left: The material exhibited iridescent patches in its wispy, fibrous-like structure, resembling a lava cave covered in spiderwebs. Right: The iridescence phenomenon changed as the angle of view shifted under fiber-optic illumination. Fields of view 3.60 mm (left) and 1.88 mm (right).

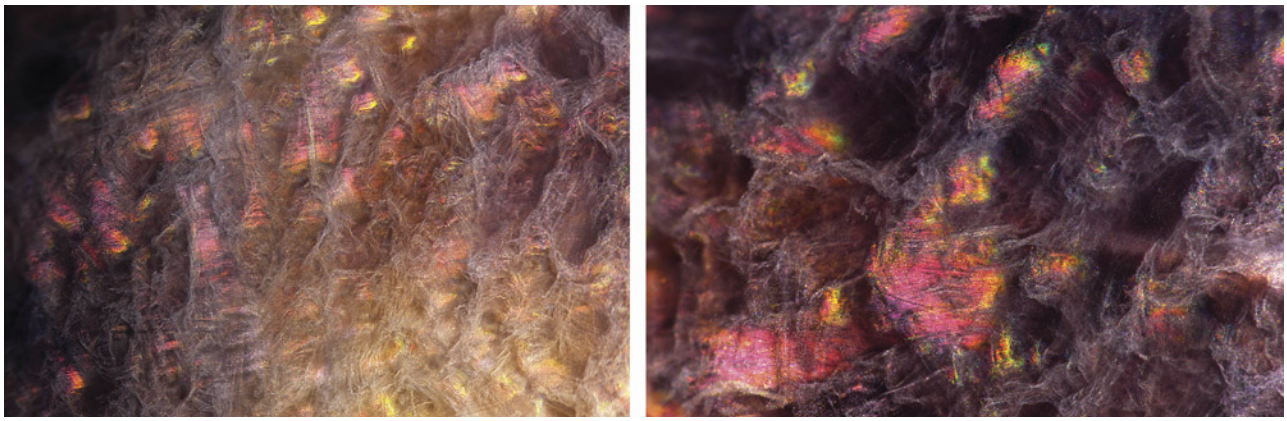

as the item was moved and turned in the light (figure 22, right).

Observed externally were both a banding feature (commonly found in shell-related materials) and numerous lines across the base indicating it had been worked and altered from its original form. Real-time X-ray microradiography also revealed a distinct banded internal growth structure and parasite tubes. Raman spectroscopy identified this imitation pearl as calcite, and its bodycolor was likely treated. All this evidence, combined with energy-dispersive X-ray fluorescence analysis, indicated that the material was not a whole pearl but likely fashioned from the shell of a marine organism.

Although GIA has encountered a variety of imitation materials, this is the most fascinating specimen seen by the author.

Ravenya Atchalak

Irradiated and Dyed Akoya Pearls

Since the 1960s, irradiation has been a known treatment for modifying the color of freshwater cultured pearls (Developments and Highlights at the Gem Trade Lab in Los Angeles, Spring 1967 *G&G*, pp. 153–154). It was found that freshwater shells and pearls contained higher amounts of manganese, which could be oxidized by irradiation to produce a darkened color (T. Tsujii, "The change of pearl colors by the irradiation with γ-ray or neutron ray," *Journal of Radiation Research*, Vol. 4, No. 2-4, 1963, pp. 120–125). While saltwater pearls contain much less manganese than freshwater pearls, cultured saltwater akoya pearls could also be treated with irradiation. During treatment, the freshwater shell bead nuclei inside these cultured pearls would turn darker and cause the surface color, luster, and overtone to change (Winter 1988 Gem Trade Lab Notes, p. 244).

Recently, GIA's New York laboratory obtained two groups of reportedly irradiated akoya pearls from two different vendors. These samples were either drilled or partially drilled, ranging from 3.82 mm to 8.15 mm in diameter and from 0.29 to 3.58 ct in weight (figure 23). They exhibited a variety of light to dark-toned gray with bluish and greenish bodycolors, with variously colored overtones.

Figure 23. The two groups of reportedly irradiated akoya pearls used in this study.

Real-time X-ray microradiography and energy-dispersive X-ray fluorescence confirmed that these were bead cultured pearls grown in a saltwater environment. No silver content was detected on any of the surfaces, suggesting that the colors of these pearls had not been modified by silver nitrate treatment. Upon microscopic examination, however, some of the samples displayed obvious color concentrations at their drill holes or unnatural patchy surface color distributions, while also revealing a darkened bead nucleus inside. On the other hand, some light-colored pearls did not possess color concentrations at the drill hole and only contained a darkened bead nucleus (figure 24).

To further investigate the color origin, we cut several samples as well as a typical white akoya cultured pearl to compare their internal appearances (figure 25). The results confirmed that the reportedly irradiated pearls contained darkened bead nuclei showing brownish stripes rather than the usual white bead nucleus found in a white akoya pearl, indicative of irradiation treatment (Winter 1988 Gem Trade Lab Notes, p. 244). In addition, some samples exhibited a distinctly different color appearance at the nacre and drill-hole areas, indicating dye treatment.

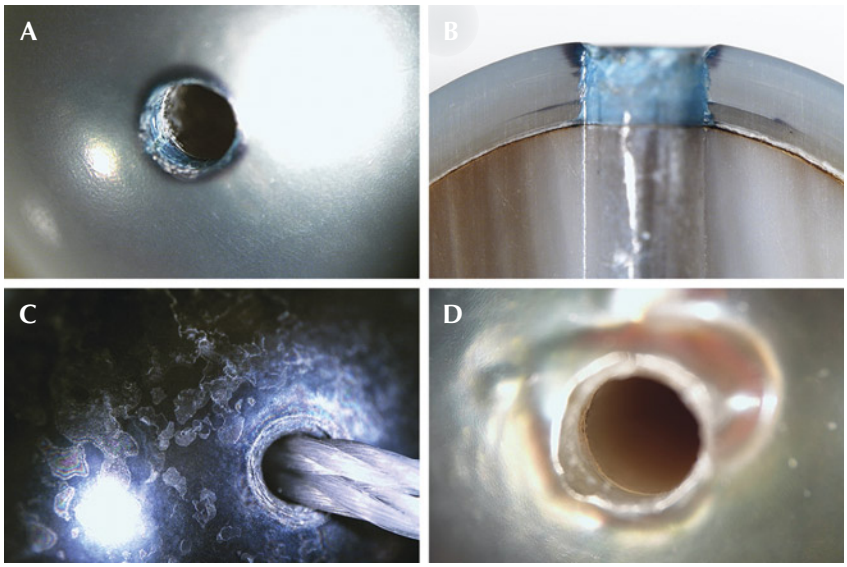

Figure 24. Images showing obvious color concentrations at the drill holes of some samples with darkened bead nuclei (A and B), an unnatural dark patchy surface (C), and a darkened bead nucleus without color concentration (D). Fields of view 4.79 mm (A and C) and 3.57 mm (B and D).

Short-wave UV fluorescence spectroscopy confirmed that the akoya pearls may have been treated by any number of processes (C. Zhou et al., "Detection of color treatment and optical brightening in Chinese freshwater 'Edison' pearls," Summer 2021 *G&G*, pp. 124–134), based on low fluorescence counts at around 320–360 nm. Raman spectroscopic analyses using 514 nm laser excitation revealed aragonite as the main component. Some treated pearls exhibited a series of unusual Raman shift peaks between 560 and 3200 cm^{-1} on the nacre (probably due to dye materials) but not on the darkened shell bead nucleus, suggesting two forms of treatment: dyeing and irradiation (figure 26).

Figure 25. Left to right: Cross sections of an irradiated akoya pearl, a white akoya pearl, and an irradiated and dyed akoya pearl. Field of view 14.52 mm.

Figure 26. Raman spectra of one sample's surface nacre, nacre on the cross section, and bead nucleus, along with the surface nacre of a white akoya pearl for comparison. Unusual peaks were found in both nacre areas but not on the bead nucleus. Also shown are typical aragonite features at 702, 704, and 1086 cm^{-1}.

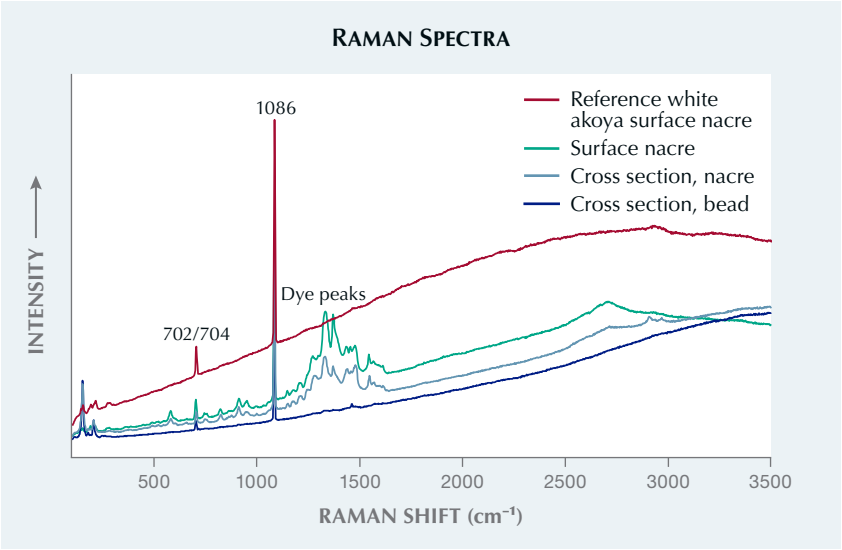

Naturally colored gray pearls are usually light in color and tend to show uneven color distribution, making them difficult to match. Some grayish akoya pearls on the market have been treated to imitate these natural colors, since they command higher prices. While dye treatments are more easily detected by unnatural bodycolors, obvious color concentrations, and advanced testing, irradiation treatment is harder to detect since the nacre is not affected and the difference in bodycolor is subtle. Careful visual observation is necessary. The combination of irradiation and dye treatments in some of these treated pearls is not commonly encountered in our laboratory.

Emiko Yazawa and Chunhui Zhou

"Lily Pad" Structure in an Orangy Yellow Pearl

GIA's Mumbai laboratory recently received for identification an orangy yellow semi-baroque pearl weighing 4.14 ct and measuring 9.51 × 8.43 × 7.51 mm (figure 27). Externally, the pearl had a distinct indentation on its

Figure 27. The orangy yellow pearl weighing 4.14 ct and measuring 9.51 × 8.43 × 7.51 mm.

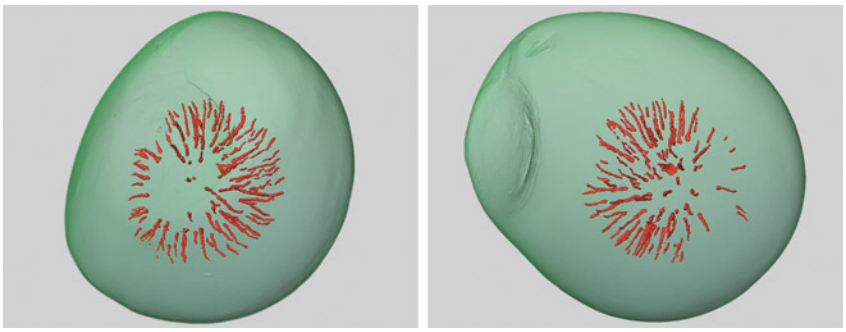

Figure 29. The 3D models generated using µ-CT scans show the acicular feature in red resembling a lily pad with a small core at the center, while the green area represents the pearl's growth structure.

top portion and possessed a medium surface luster. Observation of the surface under 40× magnification showed typical fine overlapping platelets of aragonite.

Energy-dispersive X-ray fluorescence revealed a manganese level below detection limits and a strontium level of 1226 ppm. When exposed to X-ray fluorescence, the pearl showed an inert reaction. Both results confirmed the pearl's saltwater origin. Under long-wave ultraviolet light, it exhibited a yellowish green reaction. Raman analysis using a 514 nm laser excitation revealed a doublet at 701 and 704 cm^{-1} and a peak at 1085 cm^{-1}, indicating the presence of aragonite. Photoluminescence spectra revealed two strong broad peaks at 620 and 650 nm as well as one weak peak at 680 nm, confirming the pearl's natural color origin.

Upon further testing using real-time X-ray microradiography (RTX), the pearl displayed an unusual acicular feature resembling the shape of a lily pad, with tiny flame-like structures radiating from the center. This feature was intersected by several growth arcs (figure 28A). X-ray computed microtomography (µ-CT) provided a more detailed view, revealing a distinct small void at the center. Surprisingly, the acicular "lily pad" feature observed in the RTX images appeared as numerous elongated, spiky structures with very fine lines cutting through the shape (figure 28, B and C).

To further study this feature, three-dimensional models were created using specialized software to render the µ-CT scan images (C. Zhou et al., "New 3-D software expands GIA's pearl identification capabilities," *GIA Research News*, May 13, 2016). In both the µ-CT scan images and the 3D models shown in figure 29, it was evident that this unique feature was confined to the central part of the pearl and did not extend to the outer nacre layers. Notably, the lily pad feature had elongated spikes that were thicker at one end and gradually tapered as they radiated outward from the center.

Gemological laboratories do encounter pearls with internal structures that are very difficult to positively identify. Due to the lack of conclusive evidence proving it was a cultured pearl combined with the presence of a rare and distinctive nat-

Figure 28. A: RTX image revealing a unique acicular "lily pad" feature with tiny flame-like structures. B: µ-CT scan displaying a small central core with elongated spiky features. C: A magnified µ-CT scan showing the spiky features surrounded by prominent growth arcs.

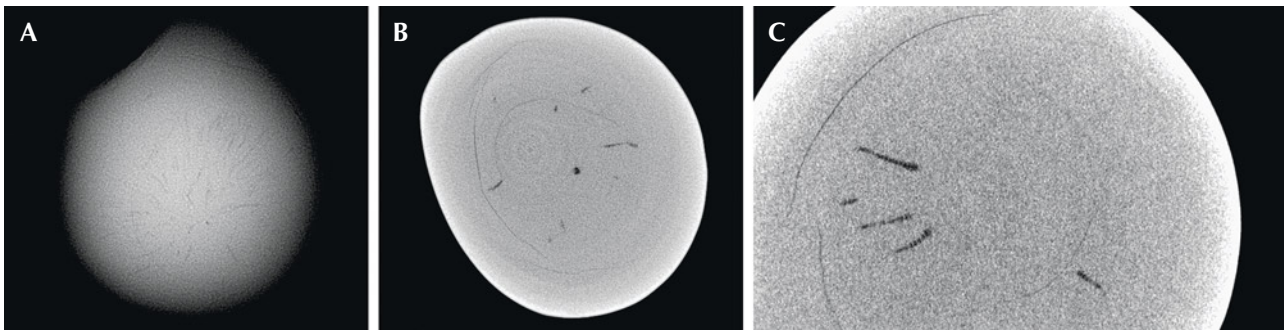

ural structure, this pearl was considered noteworthy. Such intriguing natural growth structures can be influenced by several factors, including environmental conditions, the health of the mollusk during formation, and other external causes impacting the pearl formation process. The precise mechanism of natural pearl formation continues to be widely debated, and encountering such pearl samples causes us to further contemplate the creation of these exquisite gems.

Anukul Belanke, Roxane Bhot Jain, Emiko Yazawa, and Abeer Al-Alawi

Figure 30. A freshwater shell blister weighing 40.91 ct and measuring 22.79 × 20.59 × 13.21 mm.

Vaterite in Freshwater Natural Shell Blister

A cream-colored baroque-shaped shell blister with a light orange base, weighing 40.91 ct and measuring 22.79 × 20.59 × 13.21 mm, was recently submitted to GIA's Mumbai laboratory for identification (figure 30). Externally, the large shell blister had a botryoidal arrangement with deep grooves. Viewed under 40× magnification, its high-luster surface displayed a typical nacreous structure of overlapping aragonite platelets. The base of the shell blister was sawn and polished, revealing concentric arcs and numerous polishing lines. Real-time X-ray microradiography (RTX) and X-ray computed microtomography (μ-CT) showed a distinct pattern of concentric growth arcs that terminated at the base. This was accompanied by an array of fine lines opposite the direction of the growth arcs forming grooves within the pearl (figure 31, A and B).

X-ray fluorescence (XRF) revealed a strong yellowish green reaction, indicative of its freshwater origin, with a small patch of reddish orange fluorescence observed at one end (figure 31C). Reddish orange fluorescence has been associated with vaterite in freshwater pearls (U. Wehrmeister et al., "Vaterite in freshwater cultured pearls from China and Japan," *Journal of Gemmology*, Vol. 30, No. 7/8, 2007, pp. 399–412). Further chemical analysis using energy-dispersive X-ray fluorescence spectrometry was conducted on multiple spots. The yellowish green area yielded manganese levels ranging from 261 to 504 ppm and a strontium level of 413 to 452 ppm, while the reddish orange spot had a manganese level of 323 ppm and a strontium level of 415 ppm. Raman spectroscopy using 514 nm laser excitation on multiple surface spots revealed a combination of two calcium carbonate ($CaCO_3$) polymorphs: aragonite and vaterite. The spot with reddish orange fluorescence had vaterite peaks at 752, 1075, and 1090 cm^{-1}; the areas with a yellowish green fluorescence showed peaks at 701, 704, and

Figure 31. A: RTX image showing banded structures. B: μ-CT image revealing arcs. C: X-ray fluorescence shows yellowish green fluorescence along with the reddish orange spot, indicating the presence of vaterite.

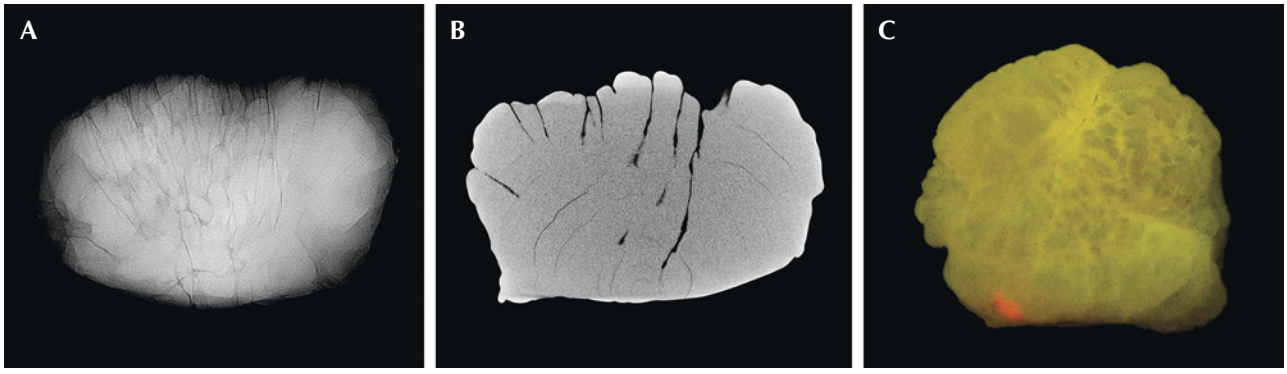

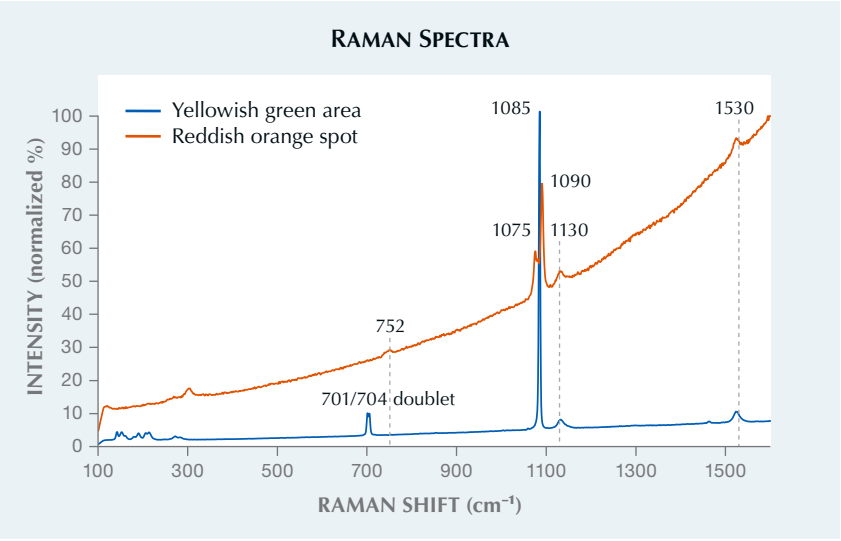

Figure 32. Raman analysis of shell blister spots fluorescing yellowish green and reddish orange under XRF revealed the presence of aragonite and vaterite peaks, respectively.

1085 cm^{-1}, indicative of aragonite, along with polyenic pigment peaks at 1130 and 1530 cm^{-1} (figure 32). The photoluminescence spectra were consistent with the Raman and displayed strong fluorescence.

The presence of vaterite in association with aragonite in freshwater pearls has been extensively researched and recorded both in natural and cultured pearls. These minerals have also been occasionally documented in mollusk shells. It is therefore interesting to see such dual mineral phases in shell blisters as well. While it has often been speculated that vaterite serves as a precursor to aragonite during biomineralization, the presence of this mineral on the periphery suggests simultaneous formation within the shell blister (A.L. Soldati et al., "Structural characterization and chemical composition of aragonite and vaterite in freshwater cultured pearls," *Mineralogical Magazine*, Vol. 72, No. 2, 2008, pp. 579–592). In certain cases, the presence of vaterite can be very difficult to detect through XRF analysis, especially when located within or around the core of the pearl. However, vaterite is more visible when the pearl is cut (Summer 2021 Gem News International, pp. 171–174).

Distinguishing between a natural blister pearl and a natural shell blister can be very challenging for laboratories due to the subtle variations in the definitions of these terms. Although such identifications are always debatable, the examined item was identified as a natural freshwater shell blister based mainly on its structural composition, external appearance, and distinct worked base, in addition to its notably large size.

Pfokreni Nipuni, Abeer Al-Alawi, and Nishka Vaz

Pearls from the Placunidae Family (Windowpane Oysters)

Nacreous pearls are commonly constructed from layers of stacked aragonite platelets. In recent years, however, GIA laboratories in Bangkok, Hong Kong, Mumbai, and New York have reported unusual pearls with a "nacreous-looking" surface caused by the presence of calcite instead of aragonite (figure 33) (Winter 2022 Lab Notes, pp. 477–478). These findings piqued curiosity and prompted a more comprehensive study involving research samples and

Figure 33. Two loose pearls from windowpane oysters submitted to the Bangkok laboratory and a mixed strand containing mostly windowpane and Pteria *species pearls submitted to the New York laboratory.*

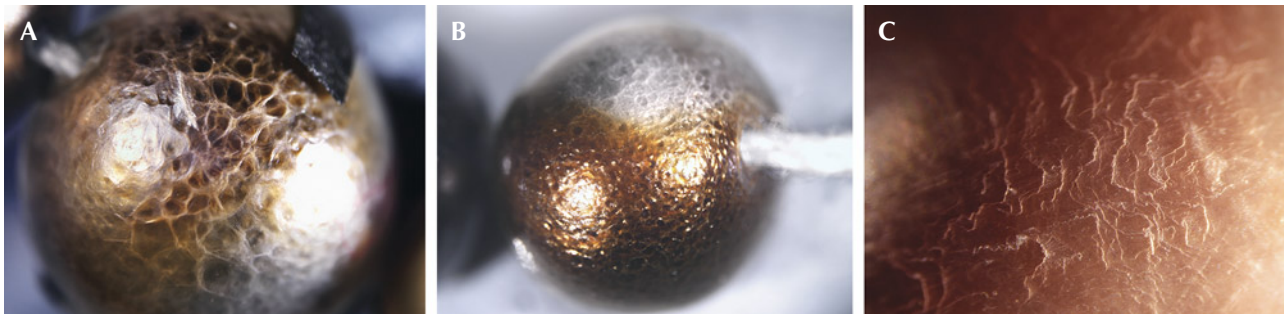

Figure 34. Characteristic surface features of mosaic pattern (A) and botryoidal structure (B) were observed on a pearl from the necklace in figure 33, compared to the typical nacreous-looking surface of fingerprint-like platy structure (C) on a loose pearl. Fields of view 7.19 mm, 9.61 mm, and 2.90 mm, respectively.

mollusk shells. The study indicated that these calcite "nacreous-looking" pearls were likely produced by mollusks belonging to the *Placuna* genus in the Placunidae family.

These marine bivalve mollusks, commonly known as "windowpane oysters," are found along the coasts of India, Malaysia, China, and the Philippines (C.M. Yonge, "Form and evolution in the Anomiacea (Mollusca: Bivalvia)-*Pododesmus*, *Anomia*, *Patro*, *Enigmonia* (Anomiidae): *Placunanomia*, *Placuna* (Placunidae, fam. Nov.)," *Philosophical Transactions of the Royal Society of London*, Vol. 276, No. 950, 1977, pp. 502–503). *Placuna* mollusks are widely valued for their thin, durable mica-like translucent flat shells, called *capiz* or *kapis* shells, which were once a popular alternative to glass and often used as windowpanes and decorations. Although the mollusks were also known to produce small pearls, these were not commercially available until recent decades (C.T. Achuthankutty et al., "Pearls of the windowpane oysters, *Placuna placenta*," *Mahasagar*, Vol. 12, No. 3, 1979, pp. 187–189).

The studied pearls were variously shaped, measuring 3 to 8 mm and weighing 1 to 3 ct. Their bodycolors ranged from silver to brown or gray, with varying degrees of tone and saturation. Viewed under 40× magnification, they exhibited diagnostic surface features of distinctive mosaic or cellular patterns, and some appeared similar to a botryoidal structure. While these features are unique and have not been observed in typical nacreous pearls, a few of the samples also showed overlapping platelets typically found in nacreous pearls (figure 34).

Under long-wave ultraviolet radiation, the pearls displayed a striking reddish fluorescence, particularly from the darker areas, which is comparable to the reactions observed on the windowpane oyster shells (figure 35). Similar reddish fluorescence has been observed in dark pearls from the *Pteria* species (L. Kiefert et al., "Cultured pearls from the Gulf of California, Mexico," Spring 2004 *G&G*, pp. 26–38; Winter 2014 Lab Notes, pp.

Figure 35. Three variously colored windowpane shells and a brown windowpane pearl, shown in daylight (left) and long-wave UV light (right). Shells courtesy of Robin Willis.

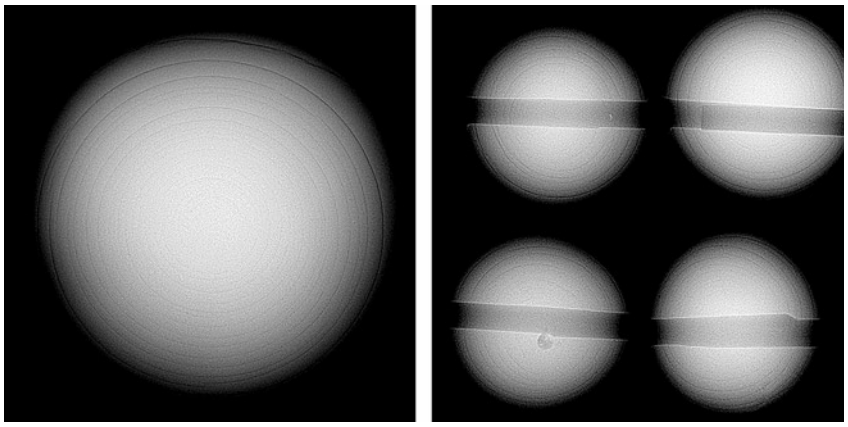

Figure 36. RTX images revealed concentric growth rings typical of the internal structure commonly observed in windowpane oyster pearls.

295–296). However, it is important to note that the composition of calcite in windowpane pearls and aragonite in *Pteria* species can be distinguished using Raman spectroscopy.

Ultraviolet/visible (UV-Vis) reflectance and photoluminescence (PL) spectra from a laser excitation at 514 nm collected on the darker areas unveiled features similar to those typically observed in natural dark nacre of *Pteria* species, as well as *Pinctada margaritifera* and *Pinctada maxima*. The UV-Vis spectra exhibited absorption features at 405 and 495 nm. The 405 nm feature is related to uroporphyrin, a type of pigment responsible for gray to black tones in some pearl oyster species (Y. Iwahashi and S. Akamatsu, "Porphyrin pigment in black-lip pearls and its application to pearl identification," *Fisheries Science*, Vol. 60, No. 1, 1994, pp. 69–71). All the samples showed bands at approximately 620, 650, and 680 nm in their PL spectra. These three PL bands have been commonly recorded in darker-colored pearls from the species mentioned above.

The saltwater origin was confirmed by energy-dispersive X-ray fluorescence spectrometry, which revealed very low or below detection limit manganese content and high levels of strontium ranging from 1000 to 1500 ppm.

Intriguingly, real-time X-ray microradiography (RTX) uncovered a distinct, evenly spaced fine concentric ring structure throughout most of the inner area of the pearls (figure 36). This structure was identified in most of the submitted pearls as well as the research samples studied. With these combined unique characteristic features, we were able to confidently conclude that the mollusks producing these pearls were from the Placunidae family. The first GIA Pearl Identification report for a pearl from this mollusk was issued in May 2023.

While most shelled mollusks have the potential to produce pearls, identifying the exact species remains a challenge, particularly with less commonly encountered species. Conducting continuous research studies with known samples from reliable sources is crucial and greatly assists in identification. As a continuation of this lab note, a comprehensive article featuring detailed studies will be prepared.

Joyce Wing Yan Ho, Kwanreun Lawanwong, and Artitaya Homkrajae

Exceptionally Rare TITANOHOLTITE

A first-time submission of a rare dumortierite supergroup member was recently examined at the Carlsbad laboratory. A 0.85 ct titanoholtite (figure 37) was identified after extensive testing. The stone was submitted as dumortierite, but its physical properties and chemistry did not support this. The dark orangy brown stone had a hydrostatic specific gravity of 3.65 and a refractive index of 1.720–1.740 (birefringence of 0.020). These properties stand in contrast to dumortierite, which usually forms as an inclusion rather than a single crystal and typically has a blue to violet color, a specific gravity of 3.21 to 3.41, and a refractive index of 1.659

Figure 37. A 0.85 ct oval modified brilliant titanoholtite. Although its bodycolor was dark orangy brown, a bluish haze was visible from certain angles due to light scattering off polish lines as well as internal colorless graining.

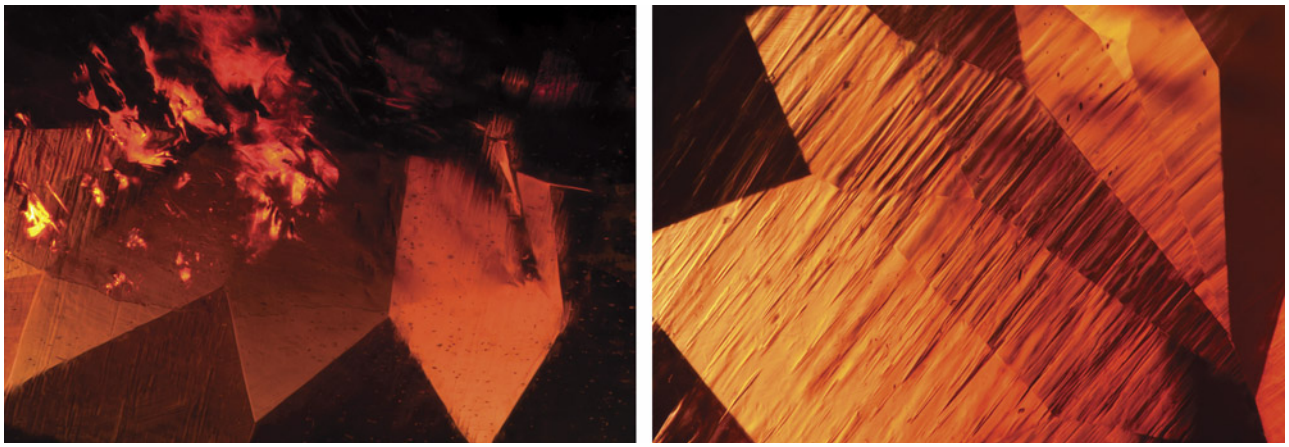

Figure 38. Left: A clean and reflective surface-reaching fracture was seen under the table; field of view 3.57 mm. Right: Abundant transparent graining, scattered particles, and thin films were seen throughout the stone; field of view 2.34 mm.

to 1.692 with a birefringence of 0.027.

A look into the stone offered a vibrant scene composed of a reflective surface-reaching fracture breaking the crown (figure 38, left) and an abundance of transparent graining throughout with small flecks of reflective thin films and unidentified particles (figure 38, right). Microscopic observation revealed a strong resemblance to garnet, but the material's doubly refractive nature was inconsistent with garnet. Raman spectroscopy results did not match any existing minerals within GIA's reference databases, but they did show some general similarities with dumortierite. Finally, laser ablation–inductively coupled plasma–mass spectrometry was performed on the stone for a full quantitative chemical analysis. Given the general similarities with dumortierite, the chemical data was fit to a dumortierite supergroup formula of $(Al_{0.35}Ti_{0.41\square 0.24}Fe_{0.02})Al_6B(Si_{2.60}Sb_{0.32})O_{17.67}$. The dominant component in this formula is titanoholtite, $(Ti_{0.75\square 0.25})Al_6BSi_3O_{18}$, with minor dumortierite, $Al_7BSi_3O_{18}$, and incorporation of significant antimony.

Titanoholtite is a recently discovered mineral within the holtite group and a member of the dumortierite supergroup. It was first published in 2013, when microscopic crystals were found in a Polish pegmatite (A. Pieczka et al., "The dumortierite supergroup. II. Three new minerals from the Szklary pegmatite, SW Poland: Nioboholtite, $(Nb_{0.6\square 0.4})Al_6BSi_3O_{18}$, titanoholtite, $(Ti_{0.75\square 0.25})Al_6BSi_3O_{18}$, and szklaryite, $\square Al_6BAs^{3+}{}_3O_{15}$," *Mineralogical Magazine*, Vol. 77, No. 6, 2013, pp. 2841–2856). This stone submitted to GIA appears to be the first macroscopic titanoholtite specimen ever reported in the literature.

Britni LeCroy and Aaron Palke

PHOTO CREDITS

Jian Xin (Jae) Liao—1, 15, 33; 5; Robert Weldon—3 (inset); Paul Johnson—4; A'Dhi Lall—6; Momo Matsumura—8; Shunsuke Nagai—9; Rambod Bahadory—10–12; Raju Jain—13; Suvarna Gaikwad—14; Stephanie Persaud—16 (left); Elina Myagkaya—18; Sood Oil (Judy) Chia—19, 23; Ravenya Atchalak—21, 22; Emiko Yazawa—24, 25; Gaurav Bera—27, 30; Pfokreni Nipuni—31 (right); Joyce Wing Yan Ho—34 (A and B), 35 (top); Artitaya Homkrajae—34C; Kwanreun Lawanwong—35 (bottom); Adriana Robinson—37; Britni LeCroy—38